

**Lateral contact yields longitudinal cohesion in active undulatory systems**Wei Zhou , Jaquelin Dezha Peralta, Zhuonan Hao , and Nick Gravish *Mechanical and Aerospace Engineering, University of California, San Diego, California 92093, USA*

(Received 10 June 2021; accepted 11 April 2022; published 16 May 2022)

Many animals and robots move using undulatory motion of their bodies. When the bodies are in close proximity undulatory motion can lead to novel collective behavior such as gait synchronization, spatial reconfiguration, and clustering. Here we study the role of contact interactions between model undulatory swimmers: three-link robots in experiment and multilink swimmers in simulation. The undulatory gait of each swimmer is generated through a time-dependent sinusoidal-like waveform which has a fixed phase offset,  $\phi$ . By varying the phase relationship between neighboring swimmers we seek to study how contact forces and planar configurations are governed by the phase difference between neighboring swimmers. We find that undulatory actuation in close proximity drives neighboring swimmers into planar equilibrium configurations that depend on the actuation phase difference. We propose a model for stable planar configurations of nearest-neighbor undulatory swimmers which we call the gait compatibility condition, which is the set of planar and phase configurations in which no collisions occur. Robotic experiments with two, three, and four swimmers exhibit good agreement with the compatibility model. To study the contact forces and the time-averaged equilibrium between undulatory systems we perform simulations. To probe the interaction potential between undulatory swimmers we apply a small force to each swimmer longitudinally to separate them from the compatible configuration and we measure their steady-state displacement. These studies reveal that undulatory swimmers in close proximity exhibit attractive longitudinal interaction forces that drive the swimmers from incompatible to compatible configurations. This system of undulatory swimmers provides new insight into active-matter systems which move through body undulation. In addition to the importance of velocity and orientation coherence in active-matter swarms, we demonstrate that undulatory phase coherence is also important for generating stable, cohesive group configurations.

DOI: [10.1103/PhysRevE.105.054604](https://doi.org/10.1103/PhysRevE.105.054604)**I. INTRODUCTION**

The field of active matter has been inspired by the collective behavior of biological systems [1]. The principles of these systems are that individuals move through self-propulsion and that interactions occur through mechanical forces often mediated through hydrodynamic or contact forces [2]. Animal groups across scales from bacteria [3,4], insects [5,6], fish [7,8], and birds [9,10] exhibit coordinated movement patterns such as group flocking and swarming. In groups of larger animals such as birds and fish the collective movements are generated through visual sensory cues [11,12] and hydrodynamic interactions between the individuals [13–16]. However, smaller scale systems such as swimming bacteria, sperm, and worms, that often swim in higher group densities may experience repulsive contact forces in addition to fluid interactions [17–19]. The role of contact interactions has been extensively studied in simple models of active matter systems such as self-propelled rods and particles [20–23]. However, when locomotion is governed by an undulatory motion the interactions between these self-propelled systems may be influenced by phase differences in undulatory gait. In this work we study how the relationship between spatial configuration and undulatory gait parameters influence the collective behavior of active undulatory systems.

Before introducing active undulatory systems we briefly review the physical phenomena of active-matter and in particular of self-propelled particles. A self-propelled particle is an agent that possesses an internal energy reservoir which can produce propulsion (see Ref. [24] for an extensive review). Groups of these particles can then interact through hydrodynamic, short- and long-range potential, or contact forces and display collective behavior such as flocking, swarming, and incoherent motion. Interactions through contact have been extensively studied in these systems and often lead to positional and velocity alignment [22,25,26]. In most examinations of the collective physics of self-propelled particles the agents themselves are propelled through constant, time-invariant propulsion. Steering forces may vary with the environment [27–29] or the other agents' positions (as in the classic Vicsek model [30]), but still typically the propulsion is slowly modulated or constant. Furthermore, the “body” shape of these particles are typically simple spheres, rods, or ellipsoids that have no articulating components (i.e., are a single rigid body). This simplification while useful for analysis and simulation is a drastic reduction of the complexity seen in living systems that often locomote through articulated body and appendage motion.

In this work we define an active undulatory system as consisting of individuals that move through body (or discrete

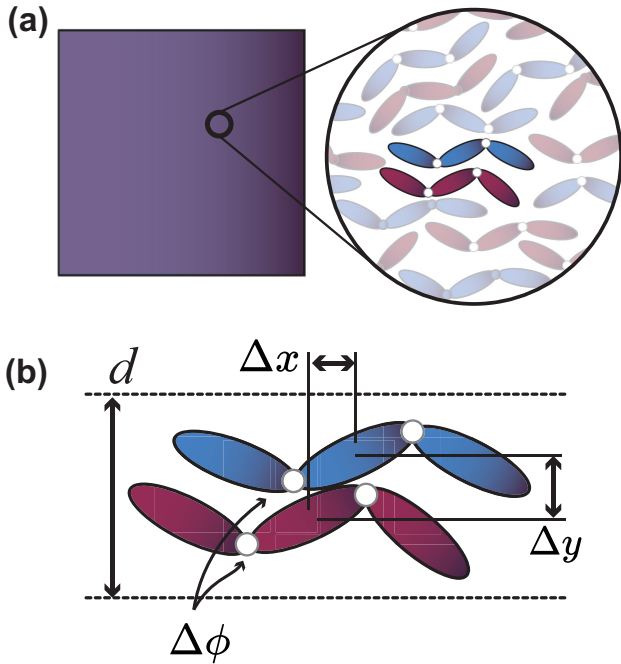


FIG. 1. Motivation and overview of gait compatibility among undulatory swimmers. (a) Large groups of swimmers experience contact interactions. (b) Contact interactions among pairs of undulatory swimmers confined to a lateral distance  $d$  require planar  $(\Delta x, \Delta y)$  reconfiguration when there is a gait phase difference  $\Delta \phi$ .

joint) bending in which bending is propagated along the length of the body. Undulatory locomotion is a common method of movement in biological systems across scales from sperm [31] to snakes [32–34]. Undulatory body bending can be three-dimensional with out-of-plane body movement such as snake sidewinding [35], however, in this work we consider planar undulatory movement. A representative undulatory gait is a simple traveling wave of body bending,  $y(x, t) = A \sin(\frac{2\pi x}{\lambda} + \omega t + \phi)$  that propagates from head to tail. The undulatory movement occurs through movement in the lateral direction,  $y$ , that propagates at wave speed  $\lambda\omega$  and with wavelength  $\lambda$  and frequency  $\omega$ . However, when considering the undulatory motion of more than one individual, an additional phase parameter  $\phi$  becomes necessary to describe the relative phases between the two systems. When swimmers have identical phases they will be in synchrony, however, when phases differ the traveling wave propagation will spatiotemporally differ which might result in forceful interactions between individuals.

The simplest system that can exhibit undulatory, traveling-wave motion is the “three-link swimmer” (Fig. 1). This system consists of three rigid links separated by two actively controlled joints. The three-link swimmer was first introduced by Purcell in his study of low Reynolds number locomotion [36] and later analyzed in Becker *et al.* in which the full dynamical equations were introduced [37]. In the many years since its introduction the three-link swimmer has been studied extensively as a model of undulatory locomotion on frictional surfaces [38,39], granular material [40], and within fluids [41,42]. Undulatory locomotion in a three-link swimmer is

generated through oscillatory motion of the two joints, whose angles  $[\beta_1, \beta_2]$  define a “shape-space” of the system [43]. A gait is defined as a closed trajectory through this shape-space over a period of time  $T$  such that  $\beta_i(t) = \beta_i(t + T)$ .

Active undulatory systems have been studied in the context of agent-environment interactions such as collision with environmental features. Undulatory robots interacting with posts display scattering phenomena that highlight the importance of active collisions between active systems and the environment [44]. These authors define active collisions as mechanical contact in which propulsive forces within the robot or animal create persistent contacts with environmental features. These active collisions yield relationships between the incoming and outgoing trajectory, dependent upon the undulatory phase and collision position. Similarly microscale swimming bacteria that locomote through reciprocal flagellar movement interact with patterned and flat walls through predictable scattering [45]. The contact interactions between flagella and the wall redirect the swimmers and the gait-phase at contact governs this scattering behavior. At a larger scale swimming nematodes (*C. elegans*) make repeated body contact with obstacles when swimming through wet granular material [46] and arrays of fixed pillars [47]. The influence of these obstructions causes the animals to change gait and to generate slower forward velocity. This previous work highlights how undulatory movement is influenced and affected by interactions with the external environment. In particular the importance of gait phase at collision suggests that the phase differences between two undulatory swimmers will play an important role in the collective physics of these systems.

This work is inspired by recent observations of collective undulatory swimming in nematodes [48], vinegar worms [49,50], and sperm. These undulatory swimmers often form clusters of high-density swimmers [17,51], and the close proximity between individuals can generate forceful interactions through hydrodynamics and contact. Hydrodynamic interactions between microscale undulatory swimmers have been well studied (see Ref. [18] for an extensive review). Interactions through a fluid can lead to long- and short-range forces that drive spatial clustering [19,52] and synchronization phenomena [53–57]. When organisms increase in size, the role of hydrodynamic interactions is diminished, yet individuals may still interact through contact. Recent experiments with vinegar worms [49,50] and nematodes [48] demonstrate that contact interactions can generate synchronization of the undulatory gait. More broadly, contact interactions between undulatory systems can generate coherent and incoherent movement dependent on density, gait, and actuation parameters [58–60].

In the following work we study the planar dynamics of undulatory swimmers in close proximity to determine the role of gait phase difference. In experiments we study the relative planar positioning of robot “swimmers” in which the individual swimmers do not “swim” but instead rest on a frictional surface. In simulations we studied swimmer groups that did swim through viscous forces acting on them. In both robot experiments and numerical simulation we find that as the phase difference between swimmers increases there is an increasing interaction “force” along the longitudinal direction that pushes swimmers to a stable planar configuration. This stable configuration is determined by the planar arrangement

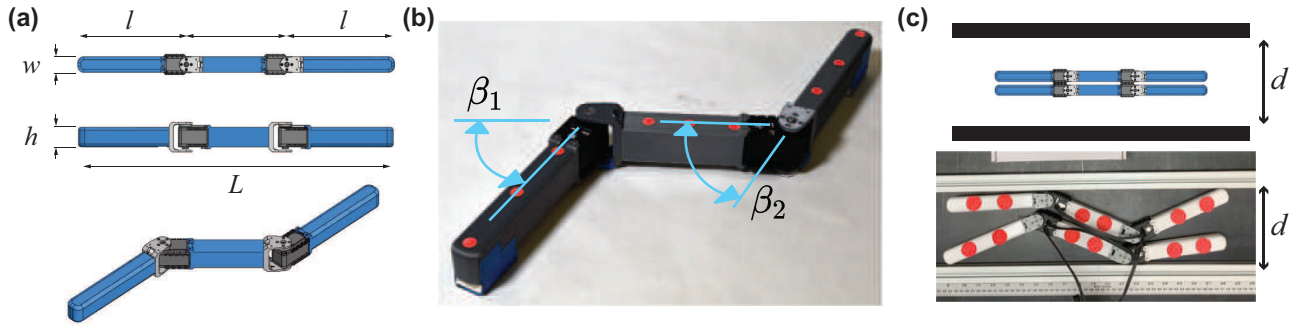


FIG. 2. Overview of three-link robots. (a) Geometry of the three-link system. Links are length,  $l = 17$  cm, height,  $h = 5$  cm, and width,  $w = 2.5$  cm. (b) The joint angles  $\beta_1$  and  $\beta_2$  are controlled through position-commanded servos. (c) We studied groups of robots in a narrow channel of variable width  $d$ .

and phase difference and is called the compatibility condition for undulatory motion. In the subsequent work we demonstrate that compatibility governs the packing arrangements of undulatory swimmers, and when swimmers are pushed out of compatibility their contact interactions attempt to drive them back to compatibility. Ultimately this work highlights the importance of contact interactions and critically gait phase on the collective behavior of active undulatory systems.

This paper is organized through a series of robophysical experiments and numerical simulation. In Sec. II we provide details for the robot experiments and numerical simulation. The first observations are made with pairs of undulatory robots in Sec. III A where we demonstrate that phase differences between undulatory robots lead to longitudinal repositioning of the robots. The details of the phase and spatial dynamics depend on actuation waveform which is studied in experiment and simulation. From these experiments we develop a model in Sec. III B of spatial configurations that depend on gait which we call *gait compatibility*. The gait compatibility model is based on an assumption of a smooth, sinusoidal body shape that differs from the three-link robots studied in experiment and simulation and thus we next study the role of body shape on compatibility (Sec. III C). We next study groups of three and four robots to observe spatial dynamics in these collectives (Sec. III D). The robot group experiments and the compatibility model suggest a packing density limitation with groups of swimmers at different phases which is investigated in Sec. III E. Lastly, in numerical simulation we observe the basins of attraction of compatible configurations (Sec. III F) and we measure the “potential energy” of these stable configurations (Sec. III G). This combination of robot experiments and numerical simulation reveal that undulatory phase differences have a significant influence on spatial configurations within undulatory active systems.

## II. METHODS

We performed robot experiments and numerical simulations to model the collective behavior of undulatory “swimmers” that have rigid links coupled through rotational joints. We studied the behavior of two and up to ten robots through experiment and simulation (Fig. 2).

### A. Robotics experiments

The robot experiment setup was designed to observe the collision interactions between two to four swimmers. Each swimmer in an experiment was comprised of a three-link robot (Fig. 2). Each robot had a three-dimensional (3D) printed body connected with two Dynamixel AX-12A servo motors [Fig. 2(a)] with a total length,  $L = 51$  cm. All servo motors were programmed to oscillate with a sine function of constant amplitude and constant frequency (0.5 Hz). The servo motors were commanded to follow an angular trajectory that was controlled with a proportional controller and a maximum torque of 1.5 N m. To produce an undulatory motion, we generated a traveling wave along the length of the body with angular position of the  $i$ th joint on the  $j$ th robot as

$$\beta_i^j = \beta_0 \sin \left( \frac{2\pi \xi i}{N} - 2\pi ft + \phi_j \right), \quad (1)$$

where  $i = \{1, 2\}$  denotes the joint number and  $N = 3$  for the three links of the robot [Fig. 2(b)].  $j = \{1, 2, 3, \dots\}$  denotes different robots. The ratio  $\xi = \frac{L}{\lambda}$  is the number of wavelengths along the body. In our experiments we varied  $\xi = [0, \frac{3}{4}, 1, \frac{3}{2}]$ . The angular amplitude,  $\beta_0$ , was held constant at  $\beta_0 = 45^\circ$  in experiment and  $\beta_0 = 40^\circ$  in simulation. We conducted a set of sensitivity analyses of the actuation parameters such as motor angular amplitude  $\beta_0$ , motor controller proportional gain  $K_P$ , and swimmer body length  $L$ , in simulation. The results were consistent across a large variation of these parameter values. The phase offset  $\phi_j$  is constant for each robot, but could differ between robots and represents the overall actuation phase of the robot. Thus the phase difference between robots is represented by  $\Delta\phi = \phi_a - \phi_b$ .

The goal of this paper is to study the spatial dynamics of undulatory swimmer groups as they swim in the same direction [Fig. 1(a)]. We emulated the effect of being within a group by confining the robots to a narrow channel so that they are forced to interact with each other. When the confining wall is not in place the robots will push each other away until they no longer contact and interact. The confined environment was created using a fixed channel measuring (slightly more than) one meter long and 13 cm wide [Fig. 2(c)]. The robots rested on a frictional surface and were confined laterally by two rigid walls whose separation distance  $d$  was varied depending on the number of robots in the experiment. When robot pairs or

groups are in the channel they are able to move laterally ( $\Delta y$ ) and longitudinally ( $\Delta x$ ) with respect to each other through contact.  $\Delta x$  and  $\Delta y$  were measured as the planar distance between the middle of the central links between each robot. Because of the constraint of the narrow channel, the rotation of robots was ignored. Each experiment consisted of placing the robots laterally in contact ( $\Delta y = 1.5$  cm) and at the same longitudinal position ( $\Delta x = 0$ ). Video recording of the robot movements was captured from an overhead view (see Supplemental Material [61]). A meter stick was aligned along the channel's length to measure the robot locations measured at each robot's center. At the start of each experiment, the two robots were set to their elongated shape, with joint angles  $\beta_i^j = 0$ .

Through video tracking we measured the center position of all robots in the experiment. We compute the center-to-center spacing between nearest neighbors to determine the lateral and longitudinal spatial shifts that occur during undulatory movement. The motors were commanded to generate an undulatory gait for 15 oscillations (30 seconds). In robot pairs this process was repeated for the varying phase shift in the two robot experiments,  $\Delta\phi$ , at values  $[-1, -0.75, -0.5, -0.25, 0, 0.25, 0.5, 0.75, 1]\pi$ . Phase shift in three robot experiments was set at values  $[-1, -0.5, 0, 0.5, 1]\pi$ . For the four robot tests the phase shifts were selected at random. We additionally performed this measurement for varying wavelengths.

The robots did not have wheels or any other frictional anisotropy and thus they do not "locomote" along a particular direction but rather undergo continuous traveling-wave oscillation while approximately remaining in the same spatial location. While the robots do not swim in experiment, our focus in this paper is the influence of contact interactions on the relative spatial positioning between undulatory swimmers. In simulations we implemented viscous drag forces on the swimmers to make them swim forward emulating being in a low Reynolds number environment. We found good agreement between the experiment and simulation. Thus, despite the robots not swimming through a fluid we believe their contact interactions are commensurate with those of the swimming systems that inspired this work.

### B. Simulation details

We performed simulations of undulatory swimmer groups to compare with experiment and to extend analysis of this system beyond what is experimentally feasible. The system was studied in the Project CHRONO multibody physics simulation environment [62]. In simulation the swimmers interacted through contact normal forces. Contact interactions in CHRONO are modeled using a discrete element method (DEM) framework. CHRONO handles two forms of DEM, one in which only "rigid" interactions occur which are handled through complementarity conditions that enforce nonpenetration between bodies (DEM-C). The second method, DEM-P, models "soft" interactions and uses a penalty-based method modeling contacts as overlapping elastic bodies with elastic interactions. In our simulations we use the DEM-C method to handle contacts. The DEM-C and DEM-P methods have been compared in Pazouki *et al.* [63] in addition to validation

comparisons. Details of the DEM-C method in CHRONO are described in the Appendix and can be found in Tasora *et al.* [62], Pazouki *et al.* [63], and Heyn *et al.* [64]. In CHRONO the swimmer links are modeled by rectangular collision shapes for collision detection. We set the tangential friction to zero and normal coefficient of restitution to zero in the simulations.

Viscous drag forces were applied to swimmer links to emulate the swimmers moving in a low Reynolds number environment [65]. The drag forces applied to the moving swimmer links are provided in the Appendix. We modeled the position-controlled servos in simulation through torque actuation of the joints under a proportional position control (P gain = 0.15 N m/rad) with torque saturation to model the maximum torque capabilities of the motors. The torque saturation in simulation was set to the same saturation of the experiment motors, 1.5 N m. The motors were commanded to follow the trajectories defined in Eq. (1). We primarily studied groups of three-link swimmers consistent with experiment. However, we did perform simulations with five-link, seven-link, and nine-link swimmers to understand how link number influenced spatial dynamics.

## III. RESULTS AND DISCUSSION

### A. Spatial reconfiguration between robot pairs

We begin our investigation by studying pairs of robots in experiment and simulation. We set the channel width to  $d = 13$  cm to constrain the robots laterally and we perform experiments with a phase difference between the two robots of  $\Delta\phi = \phi_1 - \phi_2$  over the range of  $\Delta\phi \in [-\pi, \pi]$ . We observe that robots with nonzero  $\Delta\phi$  experience a longitudinal displacement  $\Delta x$  driven by the contact interactions [Figs. 3(a) and 3(b)]. The longitudinal separation  $\Delta x$  was measured by averaging the position difference of the robot centers in the last five periods where the robots have reached a steady-state value for longitudinal spacing.

In the  $\xi = 1$  experiments a phase difference between the two robots resulted in a change in the steady-state longitudinal separation with an approximately linear relationship [Fig. 3(b)]. The slope of the  $\frac{\Delta x}{\lambda}$  versus  $\Delta\phi$  relationship was the same over different number of traveling waves along the body between  $\xi = [\frac{3}{4}, 1, \frac{3}{2}]$  [Figs. 3(b) and 3(c)]. However, when  $\xi$  was relatively large or small we observed that deviation from this linear relationship [Fig. 3(c), top and bottom panels]. Numerical simulations of two swimmers in a viscous fluid with identical geometries agreed well with the experiment.

### B. A gait compatibility model for undulatory collectives

We hypothesize that undulatory swimmers actuated through a sinusoidal traveling wave adjust their planar positioning to minimize contact interactions. We now derive a geometric relationship between phase and planar configuration based on the assumption of minimizing contact. We assume that the undulating motion of the three-link swimmer is represented by a sinusoidal traveling wave of amplitude  $A$  and wavelength  $\lambda$ , and that there is no lateral separation between the swimmers ( $\Delta y = 0$ ; we relax this assumption later). In the continuum limit the lateral position of each swimmer is

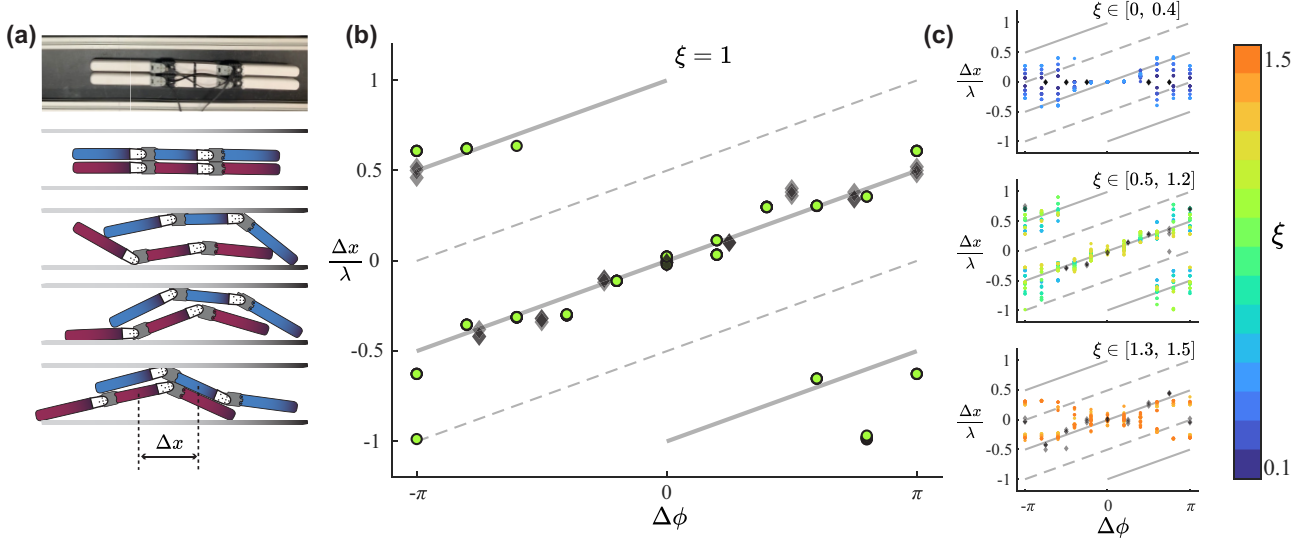


FIG. 3. Gait compatibility in undulatory swimmer pairs. (a) Image of two undulatory robot swimmers in experiment and illustration of longitudinal motion from contact interactions. Illustrations are traced from experiment images. (b) Steady-state longitudinal separation versus phase difference between robot pairs with  $\xi = 1$ . Black diamonds are experimental results; green dots are simulation results. Solid lines are compatibility predictions from equation (2). (c) The right column shows the simulation results with different  $\xi$  at three ranges. Experiment results with  $\xi = [0, \frac{3}{4}, \frac{3}{2}]$  are included accordingly. The solid lines are the compatibility prediction.

thus described by

$$y_1(x, t) = A \sin\left(2\pi \frac{x}{\lambda} + \omega t\right),$$

$$y_2(x, t) = A \sin\left(2\pi \frac{(x - \Delta x)}{\lambda} + \omega t + \Delta\phi\right).$$

We propose that an equilibrium configuration of undulatory swimmers occurs when the two sinusoidal curves make tangential contact (i.e., they are just close enough to touch but do not intersect) which is shown in Fig. 4(a). For the case of no lateral separation this imposes the single constraint,  $y_1(x, t) = y_2(x, t)$ , which can be satisfied by a relative longitudinal displacement between the two swimmers by an amount

$$\Delta x = \frac{\lambda}{2\pi} \Delta\phi. \quad (2)$$

We call this condition the compatibility condition for undulatory swimmers, inspired by recent experiments on swimming worms which introduced the term gait compatibility [48].

We plot the gait compatibility prediction along with the experiment and simulation measurements in Figs. 3(b) and 3(c) for the swimmer pairs. We find good agreement with the model prediction when the number of wavelengths along the body,  $\xi$ , is close to 1. However, as discussed in the previous section, the observations from experiment and simulation differ for large and small  $\xi$ . The gait compatibility model suggests that oscillatory swimmers with traveling-wave actuation can swim in close proximity by adjustments to their longitudinal position according to their phase difference. When  $\xi$  is small but nonzero the swimmer length is substantially smaller than the commanded wavelength. In this case deviations from compatibility can occur because the contact location predicted from sinusoidal curves is outside the range of the finite body length of the swimmers. Thus, in theory they would interact but in actuality with small  $\xi$  the interaction may not occur.

Alternatively, when  $\xi$  is large there are multiple wavelengths along the swimmer. Using a finite number of links to represent multiple wavelengths will cause aliasing problems as  $\xi$  increases which can cause poor sinusoidal curve tracking and thus deviation from the compatibility condition. This suggests the importance of traveling wave actuation which acts to couple the lateral contact with longitudinal reconfiguration. In effect the traveling wave actuation can force neighboring swimmers along the longitudinal axis and drive them into appropriate compatible states determined by phase and planar spacing. We chose  $\xi = 1$  in rest of the simulations demonstrated in this work.

In deriving Eq. (2) we did not consider the influence of a lateral separation distance  $\Delta y$  on the allowable phase and longitudinal offsets in which compatibility is achieved. However, in larger groups contact interactions may lead to density fluctuations [66]. These density fluctuations may increase the range of compatible  $\Delta\phi$ . Here we now derive the full compatibility relationship that governs the allowable lateral, longitudinal, and phase offsets for two compatible sinusoidal gaits.

We again assume two swimmers oscillating as spatial sinusoidal waves and we now include the longitudinal ( $\Delta x$ ), phase ( $\Delta\phi$ ), and lateral ( $\Delta y$ ) offsets:

$$y_1(x, t) = A \sin\left(2\pi \frac{x}{\lambda} + \omega t\right), \quad (3)$$

$$y_2(x, t) = A \sin\left(2\pi \frac{(x - \Delta x)}{\lambda} + \omega t + \Delta\phi\right) + \Delta y. \quad (4)$$

We assume that  $\Delta y > 0$  and thus swimmers that are in compatibility satisfy the equation  $y_1(x, t) \leq y_2(x, t)$  [Fig. 4(a)]. However, the boundaries of the compatible states occur when two sinusoidal curves make tangential contact, which imposes the following two constraints:  $y_1(x^*, t) = y_2(x^*, t)$  and  $y_1'(x^*, t) = y_2'(x^*, t)$ , where prime denotes derivative with respect to  $x$ , and  $x^*$  is the contact location. Solving this

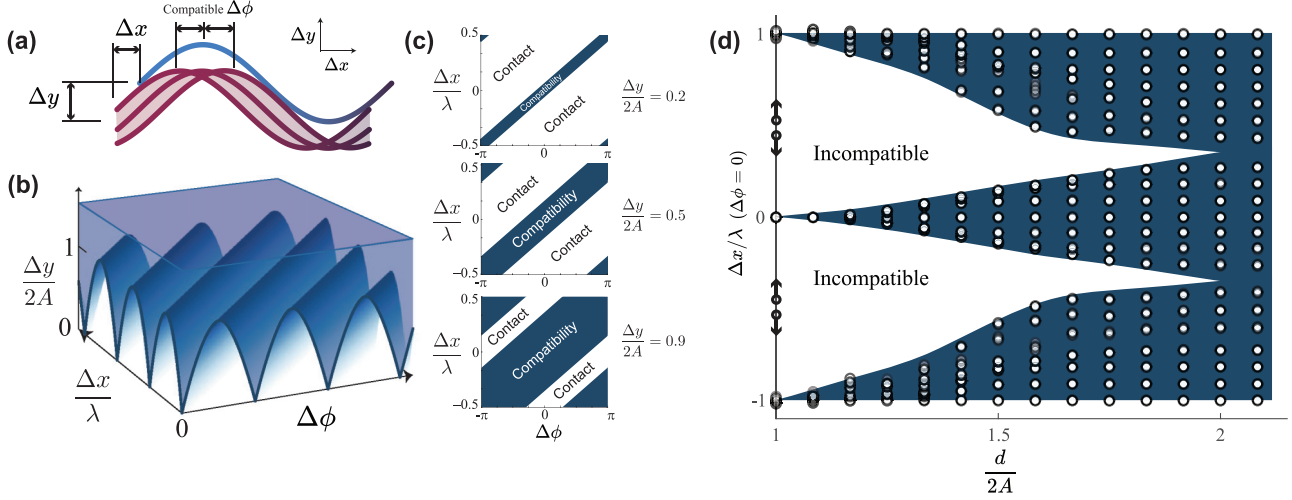


FIG. 4. Contact compatibility criteria. (a) An overview of the phase-range ( $\Delta\phi$ ) for compatible sinusoidal curves that are separated by a  $\Delta x$  and  $\Delta y$  displacement. (b) The three-dimensional representation of the compatibility criteria represented by equation (5). The shaded region above the solid blue curves are allowable configurations of gait compatibility. As the lateral separation distance increases (vertical axis,  $\frac{\Delta y}{2A}$ ) the range of compatible phases increases. (c) We show cross sections of the compatibility condition at three different lateral separations:  $\frac{\Delta y}{2A} = [0.2, 0.5, 0.9]$  from top to bottom. When  $\frac{\Delta y}{2A} > 1$  any combination of  $\Delta\phi$  and  $\Delta x$  will be in compatibility. (d) Dots indicate the steady-state longitudinal separation between two three-link swimmers in simulation with  $\Delta\phi = 0$  as a function of wall width. The shaded area is drawn to guide the eye and represents the growing compatibility region as lateral spacing is allowed to increase.

equation for the allowable phase offsets between neighboring swimmers yields the following inequality relationship:

$$\left| \Delta\phi - \frac{2\pi}{\lambda} \Delta x \right| \leq 2 \left| \arcsin \left( \frac{\Delta y}{2A} \right) \right|. \quad (5)$$

When  $\Delta y = 0$  this yields the previous equality in Eq. (2) between  $\Delta x$  and  $\Delta\phi$ . However, as  $\Delta y$  increases there is a growing range of allowable phase offsets in which two undulatory swimmers can be in gait compatibility and not make contact [Fig. 4(a)].

We show samples of the compatibility condition for varying ranges of lateral separation in Figs. 4(b) and 4(c), which highlights the growing region of compatible phase and longitudinal separation as lateral distance increases. The gait compatibility described here is somewhat similar to the hydrodynamic synchronization of infinite two-dimensional undulating sheets studied by Elfring and Lauga [67]. In that work, the two sheets could freely displace longitudinally through fluid force interactions and the authors demonstrated that the sheets always converged to a relative in-phase or antiphase configuration, depending on waveform. However, there is a critical difference between this work and the case of systems that interact through hydrodynamic forces. When two swimmers are within gait compatibility, they do not contact each other and thus are entirely decoupled. Small perturbations to their position or phase, as long as they are not pushed out of compatibility (and thus into contact), will persist, indicating that the compatibility state is a neutrally stable configuration. The interaction through contact means that there is a discontinuity at the boundary between states where the swimmers can interact, and states where they cannot interact.

To observe how the compatibility states change when the swimmer separation distance is increased we performed simulations for  $\Delta\phi = 0$  with initial conditions ranging from

$\frac{\Delta x}{\lambda} \in [-1, 1]$ . We observed the final longitudinal separation distance as a function of the initial conditions and confinement. We normalize the confinement wall distance  $d$  by the peak-to-peak oscillatory amplitude of the undulatory body wave such that, when  $\frac{d}{2A} > 2$ , swimmers through initial contact can push each other away and out of compatibility without the wall confinement to bring them back into contact. In theory, confinement distances  $\frac{d}{2A} < 1$  are not possible because the undulatory gait is obstructed. Increasing the confinement wall distance increased the range of final longitudinal spacing observed between two swimmers [Fig. 4(d)]. The central compatibility state broadened indicating that swimmers could compatibly move within a range of longitudinal separations without contact. This is in accord with the predictions from the compatibility model [Eq. (5)] in which nonzero lateral separations ( $\Delta y > 0$ ) allow for a range of solutions to the compatibility conditions. In practice there will always be lateral spacing in active assemblies and this highlights a novel aspect of contact-mediated interactions because once in the compatible state the swimmers no longer can interact until pushed back out of compatibility.

### C. Increasing link number yields better agreement with compatibility model

In both experiment and simulation we noticed that the relative equilibrium of the longitudinal spacing  $\Delta x$  formed discrete clusters along the compatibility prediction line while the prediction from a sinusoidal model is a linear phase-displacement relationship. We hypothesized that this model error was the result of the poor approximation of a sinusoidal shape by the three-link system. To determine how link number influenced compatibility we studied five-, seven-, and nine-link swimmer pairs in simulation and we found that increasing the linkage number produced an increasingly linear

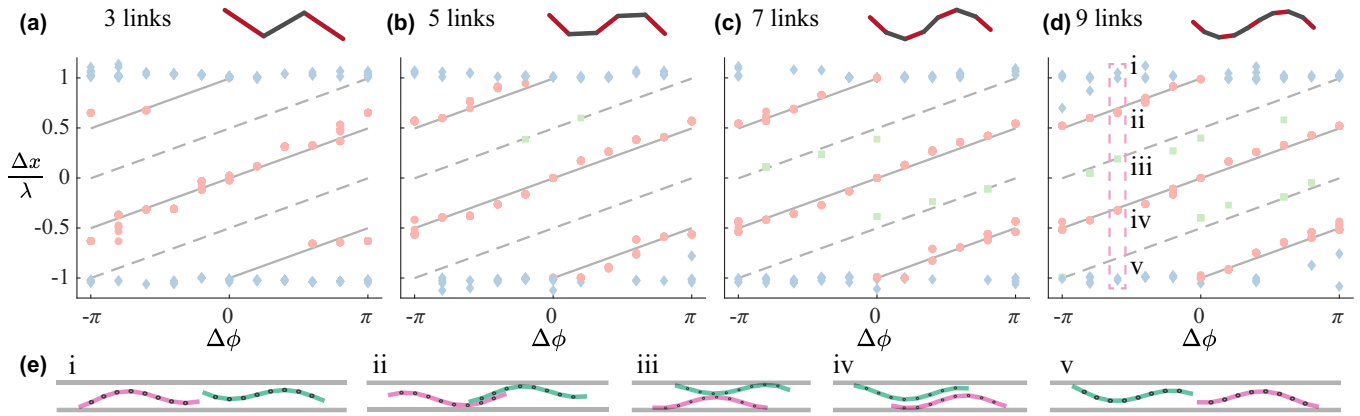


FIG. 5. (a)–(d) Gait compatibility simulations of two swimmers with 3, 5, 7, or 9 links from left to right. As the link number increases the longitudinal separation versus phase difference (red circles) show good agreement with the compatibility prediction (solid-lines). (e) Bottom figures i–v show example configurations of two nine-link swimmers. Red circles represent swimmer pairs that reached the compatibility condition (ii, iv), blue diamonds represent swimmer pairs that separate longitudinally with each other (i, v), green squares represent swimmer pairs that are jammed with each other (iii).

compatibility relationship with increasing link number [Fig. 5]. The root mean square (rms) error of the simulation compatibility separation and the prediction [Eq. (2)] decreased with increasing link number (rms error from compatibility condition = [0.084, 0.063, 0.044, 0.039] for the [3,5,7,9] link swimmers, respectively). The decreasing error with increasing link number is a result of the discretized body-shape in the three-link swimmers. The compatibility model assumes a perfectly sinusoidal body shape, however, with only three links the body undulation is not quite sinusoidal. However, as we add more links this assumption becomes better so does the gait compatibility model.

#### D. Experiments with three and four robot pairs

To examine how larger groups of undulatory swimmers arrange spatially we performed experiments with groups of three and four robots [Fig. 6(a)]. We widened the channel to  $d = 19$  and  $22$  cm for three- and four-robot experiments and set  $\xi = 1$ . The robots are initialized with  $\Delta x = 0$  and all joint angles set to zero. We begin undulatory actuation for the robots and we monitor the lateral and longitudinal displacement from an overhead camera [Fig. 6(a)]. We observed the same overall behavior in robot groups as in robot pairs: phase differences between neighboring robots resulted in longitudinal repositioning until the group reached an overall steady-state spatial configuration. Examining the nearest neighbor  $\Delta x_{i,i+1}$  versus  $\Delta \phi_{i,i+1}$  we observe reasonably good agreement with the compatibility predictions [Fig. 6(b)]. However, in both the three- and four-robot groups we do observe relationships of  $\frac{\Delta x}{\lambda}$  vs  $\Delta \phi$  that lie in between the compatibility states [dashed line in Fig. 6(b)]. Visual inspection of these experiments suggests that these data points represent configurations that are effectively “stuck” in between the two compatible configurations. In states lying along the dashed line it requires an equidistant longitudinal shift in either the positive or negative to reach compatibility, and thus the interactions that drive the robots to compatibility may conflict along this line and cause them to remain stuck. These dynamics will be explored further in Sec. III F.

The variation in the longitudinal position was larger in the group experiments compared with the robot pair experiments suggesting potential collective effects present in the three-

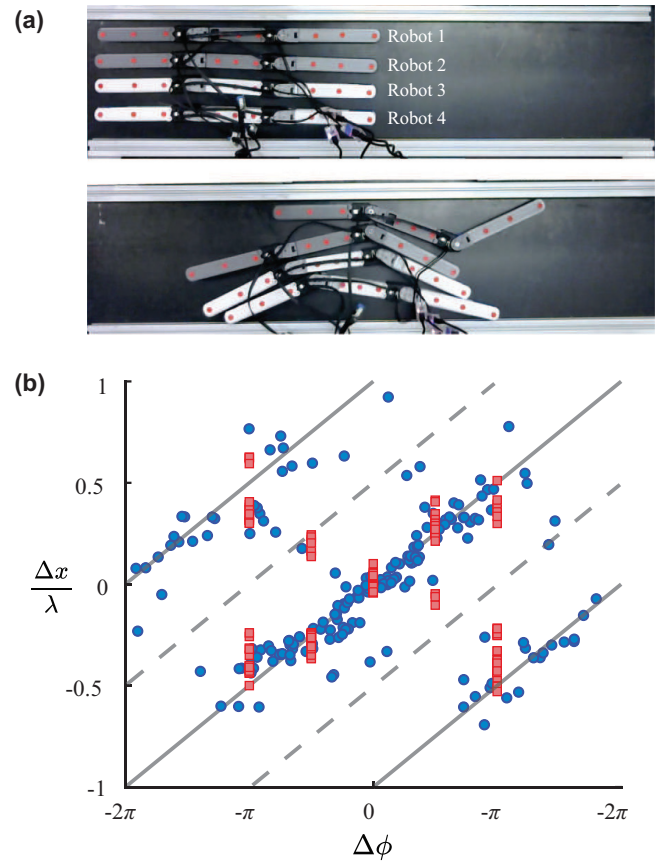


FIG. 6. Gait compatibility in larger robot groups. (a) Image of a four-robot experiment at the beginning (top) and in the middle of the experiment (bottom). (b) Steady-state longitudinal separation versus phase difference groups experiments with three (red squares) and four robots (blue circles). Solid lines are compatibility predictions from Eq. (2).

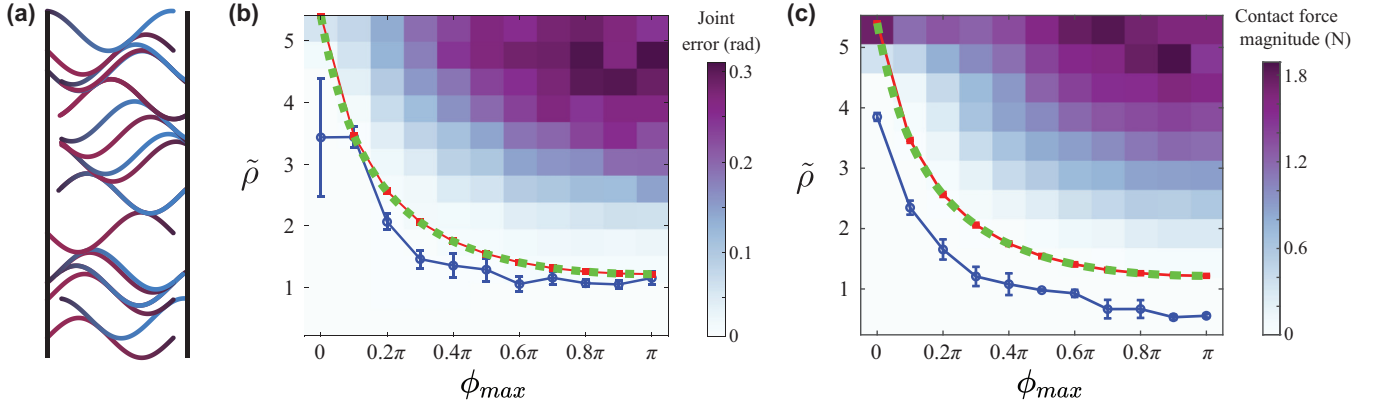


FIG. 7. Lateral density is influenced by phase variance in undulatory groups. (a) A representation of a group of undulatory swimmers separated laterally (the vertical direction) in tangent contact with phase variation. (b) A heatmap of time-averaged absolute value of joint error induced through collisions within a swimmer group for varying normalized lateral density,  $\tilde{\rho}$  (y axis) and the range of phase variation (x axis). Blue circles indicate the measured joint error threshold below which contact typically does not occur in the group from simulations. Error bars represent the standard deviation of the mean taken over five periods. (c) A heatmap of time-averaged magnitude of contact forces induced through collisions within a swimmer group. Blue circles indicate the baseline contact force threshold between a swimmer and the wall. Error bars represent the standard deviation of the mean taken over five-periods. In both panels (b) and (c): The red curve is a Monte Carlo estimate based on the compatibility equation. The dashed green curve is the calculation from the math model (10).

and four-robot experiments that were not captured in the pair experiments. The principal influence of this variance from the compatibility prediction is the larger lateral spacing afforded to the larger robot groups. As the swimmers push each other they may arrange into high- and low-density configurations leaving lateral space for some robots, which thus increases the range of compatible phases allowable [Eq. (5)]. We explore how density influences phase variance in the next section.

### E. Gait compatibility influences spatial packing

Contact interactions among the collective undulatory swimmers drive them into compatible configurations. However, the range of available compatible configurations increases as the lateral spacing increases and thus we expect that the group density will influence the allowable phase and spatial variance in groups. To address this question we studied the packing configurations of large groups of three-link swimmers in simulation to determine the relationship between group phase variance and packing density. We used a short channel to confine the swimmers longitudinally by a distance of  $1.1L$  constraining the ability to longitudinally reconfigure. We initialized 50 three-link swimmers within a channel of fixed lateral width [Fig. 7(a)] and we measured the spatial positioning, and the deflection of the rotational joints from their commanded trajectory (joint error). The swimmers were all oriented along the direction of the channel length so that they only interacted through lateral collisions and their orientations were approximately the same. We varied the lateral confinement distance and the range of gait phases to observe how spatial and phase variance influences the packing and contact interactions between groups of undulatory swimmers.

We characterized contact interactions between swimmers by monitoring both the joint error, and the contact forces. The joint error is linearly proportional to the joint torque in the joint control system, and thus this is a metric of contact interactions between swimmers. Since joint error varies from

positive to negative through an oscillation cycle we take the absolute value of all joint errors and time average over five periods. When the swimmers are not in contact the joint error is approximately zero (viscous drag causes the error to never reach zero). However, when the lateral density is increased the swimmers begin contacting each other and causing the joints to deviate from their assigned motion. We examine the influence of phase-range and lateral density on the packing behavior of the swimmers [Fig. 7(b)]. For a fixed density, increasing the phase-range resulted in an increase in the overall joint error of the swimmers in the group indicating collisions and noncompatible space-phase relationships. Similarly, for a fixed phase-range increasing the density caused an increase in joint error.

We characterized the compatibility threshold in simulations by determining for each phase-range and density combination whether the mean joint error was above that of an individual swimmer (threshold of 0.01 rad.). The compatibility threshold from simulations is shown in blue circles in Fig. 7(b), where error bars are the result of five replicate simulations. As the lateral density or the phase range increases the mean joint error increased. The threshold curve from direct simulations appears to follow an inverse relationship between lateral density and phase range.

In addition to measuring joint error we also measured the average contact forces between swimmers in numerical simulations. We averaged the contact forces across all swimmers over five periods of oscillation to determine how large the contact interactions are. Similar to the joint error [Fig. 7(b)], we observe that, as density and phase variation increase, so does the average contact force between swimmers [Fig. 7(c)].

To investigate the relationship between gait phase variance and the lateral packing density we now model the swimmers as single-period sinusoidal curves (i.e.,  $\xi = 1$ ). We first analyzed this system through a Monte Carlo (MC) approach to estimate the phase-density threshold curve. The MC method consisted of the following steps: (1) Draw 3000 random

sample phases  $\phi_i$  from a uniform distribution between zero and  $\phi_{\max}$ . (2) Set the first sinusoid at  $y_1(x) = \sin(x + \phi_1)$ . (3) Determine the required  $\Delta y_2$  so that  $y_1$  and sinusoid  $y_2(x) = \sin(x + \phi_2) + \Delta y_2$  make tangent contact (i.e., are as closely spaced in the  $y$  direction as possible without overlap).  $\Delta y_2$  is the neutral lateral position of sinusoid  $y_2$ . (4) Repeat the previous step for all remaining swimmers with phases from the 3000 randomly drawn list. (5) The total lateral space occupied by the group is  $\Delta y_{3000}$ . The lateral packing density is given as,  $\tilde{\rho} = \frac{N}{\Delta y_{3000}}$ . We repeated the whole process above 100 times to estimate the  $\rho(\phi_{\max})$  curve reported in Figs. 7(b) and 7(c). For example, Fig. 7(a) provides a snapshot of a group of sinusoidal swimmers whose phases were randomly selected between  $[0, \phi_{\max}]$  and are in perfect tangent contact. In Figs. 7(b) and 7(c) we plot the MC estimate of  $\tilde{\rho}$  shown as the red curve. The MC estimate shows qualitative agreement with the estimated threshold from the three-link simulations.

Lastly, we perform a direct analysis of the phase-density relationship of sinusoidal curves to exactly compute the compatibility packing threshold. We assume a group of sinusoidal curves with random, uniform phase distribution in the range  $\phi_i \sim U(0, \phi_{\max})$ . We set  $\Delta x = 0$  in Eq. (5) and rearrange to the following:

$$\frac{\Delta y}{2A} = \sin\left(\frac{\Delta\phi}{2}\right). \quad (6)$$

For a swimmer group with phases drawn at random from the uniform distribution  $\phi_i \sim U(0, \phi_{\max})$  the expected swimmer separation in the  $y$  direction can be derived from Eq. (6),

$$\begin{aligned} \sum_{i=1}^N \frac{|\Delta y_i|}{2AN} &= \frac{1}{N} \sum_{i=1}^N \left| \sin\left(\frac{\Delta\phi_i}{2}\right) \right| \\ &= \int_{-\phi_{\max}}^{\phi_{\max}} \left| \sin\left(\frac{s}{2}\right) \right| f_{\text{pdf}}(s) ds, \end{aligned} \quad (7)$$

where  $s = \Delta\phi$  and  $f_{\text{pdf}}(s)$  is the probability distribution of the phase difference. Since  $\phi_i \sim U(0, \phi_{\max})$ ,  $\Delta\phi$  follows a triangle distribution between  $[-\phi_{\max}, \phi_{\max}]$  which is symmetric about the  $y$  axis:

$$\begin{aligned} \frac{\bar{y}}{2A} &= \int_{-\phi_{\max}}^{\phi_{\max}} \left| \sin\left(\frac{s}{2}\right) \right| f_{\text{pdf}}(s) ds \\ &= 2 \int_0^{\phi_{\max}} \left| \sin\left(\frac{s}{2}\right) \right| \left( \frac{1}{\phi_{\max}} - \frac{1}{\phi_{\max}^2} s \right) ds \\ &= \frac{4}{\phi_{\max}} - \frac{8 \sin\left(\frac{\phi_{\max}}{2}\right)}{\phi_{\max}^2} \\ &= \frac{4}{\phi_{\max}^2} \left[ \phi_{\max} - 2 \sin\left(\frac{\phi_{\max}}{2}\right) \right]. \end{aligned} \quad (8)$$

We now calculate the expected lateral distance  $Y$  required for a group of  $N$  swimmers, considering the swimmer body width  $w$ :

$$\begin{aligned} Y &= N\bar{y} + Nw \\ &= \frac{8AN}{\phi_{\max}^2} \left[ \phi_{\max} - 2 \sin\left(\frac{\phi_{\max}}{2}\right) \right] + Nw. \end{aligned} \quad (9)$$

Thus the expected lateral density with all swimmers in compatibility is  $\rho = N/Y$  and the density normalized by the peak-to-peak oscillatory amplitude is given by  $\tilde{\rho} = 2AN/Y$ , which yields

$$\tilde{\rho} = \frac{\phi_{\max}^2}{\frac{w}{2A}\phi_{\max}^2 + 4\phi_{\max} - 8 \sin\left(\frac{\phi_{\max}}{2}\right)}. \quad (10)$$

We see in Figs. 7(b) and 7(c) that the expected value calculation agrees extremely well with the Monte Carlo simulation. Furthermore, we can examine the extremes of the density variation and their effect on packing density. When  $\phi_{\max} = 0$  the non-normalized density becomes  $\rho = \frac{1}{w}$  which corresponds to the maximum packing density of the swimmers in contact with each other. Overall we find that, as the phase variation within a swimming group increases, the required lateral density within the group must decrease or else swimmers collide with each other. This relationship provides compelling motivation for animal and engineered swarms of swimming agents to synchronize their gaits to achieve higher density groups.

### F. Compatible configurations have a broad basin of attraction

Swimmers in noncompatible configurations are pushed into compatibility through contact interactions. In the idealized situation in which swimmers are represented by sinusoidal body position the compatible configuration is a relative equilibrium where contact no longer occurs. In this section we study how the initial longitudinal separation  $\Delta x$  and phase detuning  $\Delta\phi$  influence the final state reached by the pair of undulatory swimmers. We study this for the case of close proximity with wall separation  $d = 13$  cm where contact interactions are reinforced by the close proximity (i.e., swimmers cannot push each other away laterally).

In a first example we study the spatial evolution of five different initial conditions of longitudinal separation  $\Delta x_0$  [Fig. 8(a)]. The phases are the same for these swimmers ( $\Delta\phi = 0$ ) and so the compatible configuration is  $\Delta x = 0$ . Initial separation distances that are far away from the compatible separation ( $|\Delta x_0| > 0.3$ ) are pushed away from the  $\Delta x = 0$  compatible configuration as the swimmers repel each other along the longitudinal axis. However, when the initial separation distances are closer (approximately  $|\Delta x_0| \leq 0.3$ ) the swimmers experience an effective attractive interaction force in the longitudinal direction and ultimately end in the compatible state for their phase difference.

We study the evolution of longitudinal separation across the full range of relevant initial separation and phase differences. From each initial condition we compute the total longitudinal position change,  $\Delta x_f - \Delta x_0$  and plot the heatmap of this value [Fig. 8(b)]. Nonzero values of longitudinal position change represent scenarios where interaction forces drive the swimmer pairs to compatibility conditions. Zero values represent the attraction regions. It is interesting to note that while the only interactions between the swimmers are through repulsive contact forces, the confinement and the traveling-wave shape change results in regions of longitudinal attraction between the swimmers, effectively a cohesive force between swimmers. This attractive potential will be further studied in the next section.

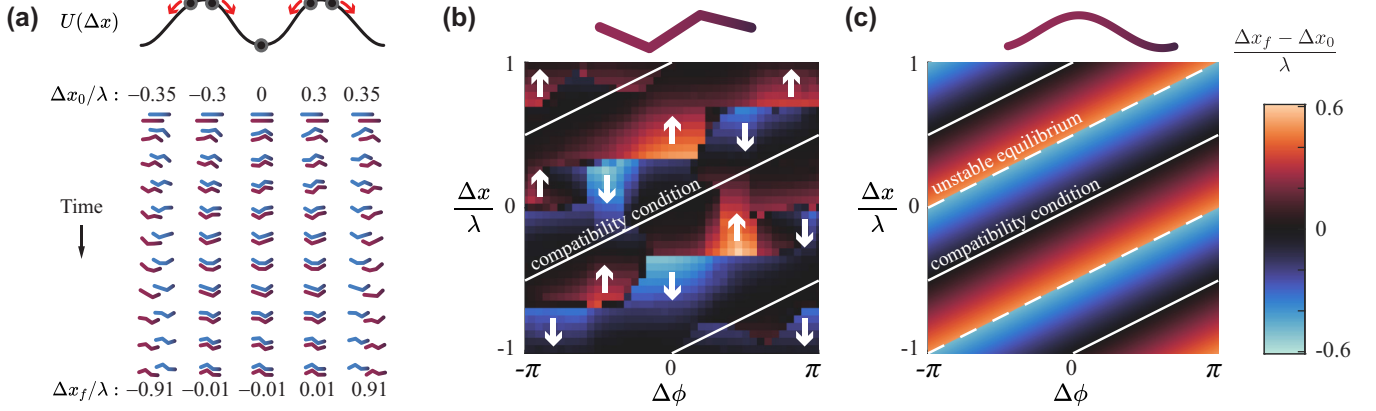


FIG. 8. Compatible configurations minimize the contact between swimmers. (a) We envision that longitudinal dynamics are governed by a potential-energy landscape dependent on the phase difference between swimmers. Swimmers initialized with  $\Delta\phi = 0$  and different longitudinal positions ( $\Delta x_0/\lambda$ ) evolve to one of three compatible configurations depending on initial position. All initial positions  $|\Delta x_0/\lambda| \leq 0.3$  evolve to  $\Delta x_f/\lambda = 0$ . (b) Heatmap represents the distance traveled from initial condition to compatibility,  $\Delta x_f - \Delta x_0$  for three-link swimmers. (c) Heatmap represents the distance traveled from initial condition to compatibility,  $\Delta x_f - \Delta x_0$  for sinusoidal swimmers. The solid lines are the compatibility lines. The dashed lines separate regions of attraction between the middle and outer compatibility lines.

From the position change map we can clearly see why the three-link swimmer experiment exhibited the clustering along the  $\Delta x$  axis [Figs. 3(b) and 5(a)]. The minimum of the interaction “potential” does not follow the sinusoidal calculation and instead follows a stair-stepped shape along the  $\Delta x$  vs  $\Delta\phi$  parameter space [Fig. 8(b)]. To determine how the three-link swimmer position change map differs from the sinusoidal prediction we compute the longitudinal position change required for two sinusoidal curves to come in to compatibility when  $\Delta y = 0$ . For two sinusoidal curves, the longitudinal displacement required to reach compatibility is the minimum  $\Delta x_f$  that results in the compatibility condition [ $y_1 - y_2 = 0$ ; from Eqs. (3) and (4)]. In Fig. 8(c) we show the displacement required to reach compatibility for two sinusoidal curves. The basins of attraction for the different compatibility lines are shown as solid lines of the same slope in Fig. 8(b). Along the dashed lines we observe that the minimum distance for compatibility undergoes a discrete change in sign. An initial condition slightly below the upper dashed line will evolve to the central compatibility line while an initial condition slightly above the upper dashed line will evolve to the upper compatibility line.

### G. Potential energy modeling of compatible configurations in simulation

To gain insight into the forces two swimmers experience when not in compatibility we performed simulations. In a first set of simulations we constrained the midpoint position (but not orientation) of two three-link swimmer’s middle link so that swimmers could interact through contact forces but could not move their central position laterally or longitudinally. We arranged swimmers with lateral separation,  $\Delta y = 3$  cm and longitudinal separation  $\Delta x = 0$ . In this arrangement  $\Delta\phi = 0$  is the compatible configuration. In a sweep of simulations we varied  $\Delta\phi$  conditions and measured the time-averaged contact forces between swimmers over five periods. The compatibility condition coincided with a minimum in the contact forces

[Fig. 9(a)] while detuning phase resulted in an increase in contact force. This observation indicates two important points: (1) as expected, contact interactions drive the spatial dynamics in this system, and (2) the system evolves to a state which minimizes the contact interactions among these active undulatory swimmers.

We hypothesize that the time-averaged contact dynamics between swimmers can be considered as an effective interaction potential with a minimum at compatibility. To measure the effective potential of the compatibility configurations in simulation we allowed two swimmers with  $\Delta\phi = 0$  to reach compatibility and then we applied a constant longitudinal separating force  $\delta F$  to each swimmer in opposing directions [Fig. 9(b)]. The separating force  $\delta F$  was applied to each swimmer by applying a force of  $\delta F/3$  to the center of mass of each link on the simulated swimmers. We observed that the swimmers separated by a longitudinal distance  $\delta x$  in the presence of this force and for small  $\delta F$  this position was sustained until the force was removed [Fig. 9(b)]. Thus, through the force perturbation we can probe the potential-energy basin of the compatible configuration for  $\Delta\phi = 0$ .

In simulation we varied  $\delta F$  and measured  $\delta x$  over a range of confinement wall distances to observe the cohesive interaction. We observed a linear relationship between the applied force and the steady-state separation, suggesting that compatible configurations act like a simple harmonic potential [Fig. 9(c)]. We fit the “stiffness” of the compatible state as  $\delta F = k(\delta x - \delta x_0)$ , where  $k$  is the interaction potential and  $\delta x_0$  is an offset. The offset  $\delta x_0$  represents the ability for systems with large enough lateral spacing to be found over a range of longitudinal separation distances ( $\Delta x$ ) when in compatibility. As we continue to increase the separating force  $\delta F$ , the average interaction force between the swimmers is no longer able to hold them together and they will separate longitudinally. In this case the swimmer pairs eventually separate and decouple from each other.

We measured the time it takes for swimmers to separate by a center to center distance of  $L$  under different forces and confinement distance. The separation time increases with

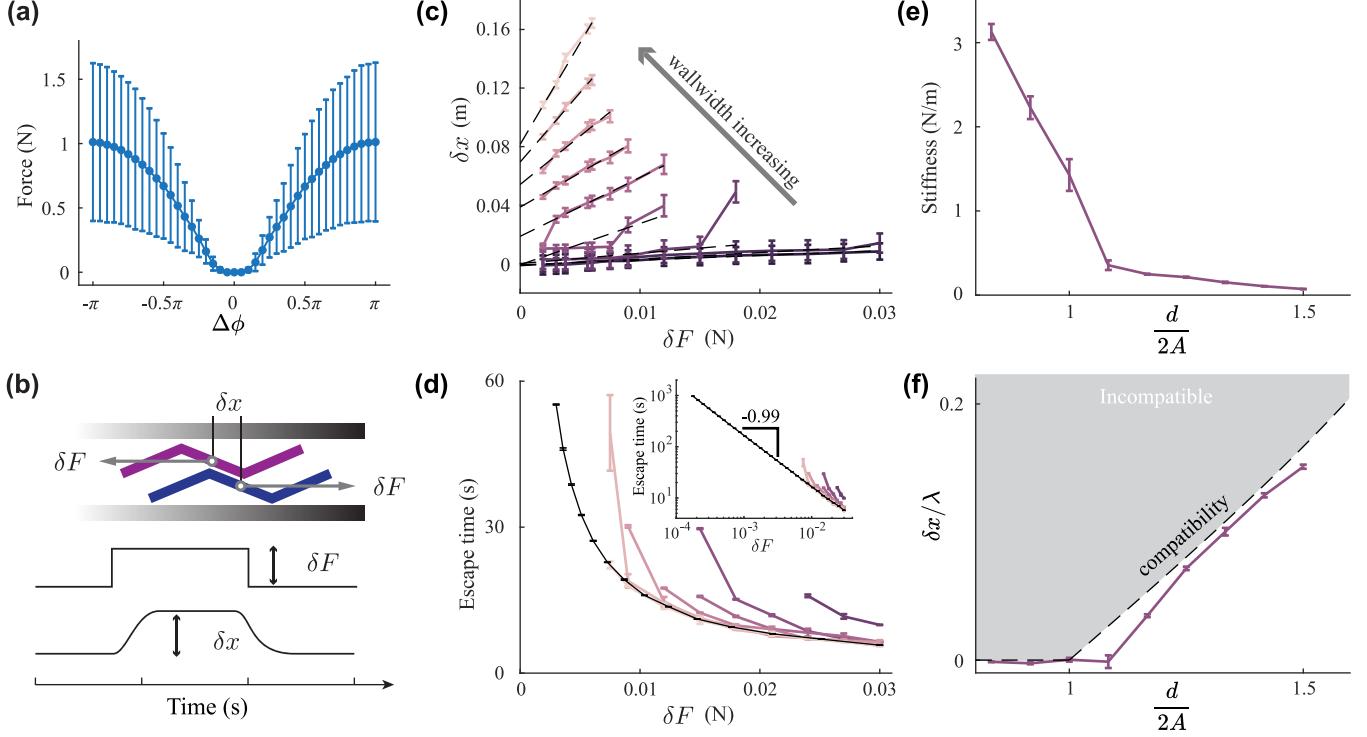


FIG. 9. Cohesive longitudinal interactions depend on confinement. (a) Magnitude of contact force between two swimmers during five periods of oscillation, with initial conditions  $\Delta x = 0$  and  $\Delta\phi$  varied from  $-\pi$  to  $\pi$ . The contact-interaction force grows with compatibility detuning. Dots represent mean contact force and error bars are standard deviation. (b) The cohesive magnitude of the compatible configuration was measured by applying equal and opposite perturbation forces  $\delta F$ . The separation distance from compatibility,  $\delta x$ , is measured. (c) Force-displacement relationship for nine confinement distances of wall widths (0.10 to 0.18 m in 0.01 m increments). Error bars represent the standard deviation of  $\delta x$  at applied  $\delta F$ . (d) Escape time for wall widths (0.12 to 0.18 m in 0.01 m increments). The black curve represents the escape time without walls. Error bars represent the standard deviation of escape time. (e) Effective interaction spring constant as a function of wall width. Error bars represent estimated spring stiffness with 95% confidence bounds. (f) Offset distance ( $\delta x_0$ ) as a function of wall width. Error bars represent estimated  $\delta x_0$  intersection with 95% confidence bounds.

decreasing  $\delta F$  [Fig. 9(d)]. When there is no lateral constraint, the escape time was estimated and shown as the black line which is linear (slope =  $-0.99$ ) on log scale as shown in the inserted plot. We can provide rationale for this inverse behavior between applied force  $\delta F$  and separation time. In the absence of contact forces the separation time can be estimated through the relationship between applied force  $\pm\delta F$  and viscous force through the following quasisteady relationship:  $\delta F = \eta_{\text{avg}} \frac{\Delta x}{\Delta T}$ . This can be reformulated into the time to separate as  $\Delta T = \eta_{\text{avg}} \frac{L}{2\delta F}$ , which displays the inverse relationship between separation time and force. In this equation,  $\eta_{\text{avg}}$  represents the period-averaged projected drag coefficient on the swimmers along the direction of motion, and  $\Delta x = \frac{L}{2}$  since both swimmers separate by  $\pm\frac{L}{2}$  to achieve a total separation of one body length,  $L$ .

We found that the cohesion stiffness  $k$  of the compatible state decreases with increasing wall width and becomes increasingly large as the confining wall spacing decreases [Fig. 9(e)]. Furthermore, the range of displacements with zero interaction force ( $\delta x_0 > 0$ ) qualitatively follows the compatibility condition [Eq. (5)], which is shown in the dashed line of Fig. 9(f). These simulations indicate that compatible states are neutrally stable configurations and a linear interaction force drives swimmers into compatibility. The boundary of

the neutral region,  $\delta x_0$ , likely lies below the prediction from the compatibility model due to the three-link geometry of the swimmers. This is similar to the comparison of the sinusoidal and three-link compatibility basins in which effects of the discrete link geometry cause the observations to deviate from theory.

#### IV. SUMMARY AND CONCLUSIONS

In this paper, we studied the role of contact interactions between undulatory swimmers in experiment and simulation. We found that contact interactions among confined swimmers drive them to stable spatial configurations called compatible gaits (originally introduced in Ref. [48]). The compatibility criteria is determined by the lateral spacing and phase difference between swimmers. We found considerable agreement between the compatibility model prediction and the experiment and simulation results. Compatible gaits are relative equilibrium configurations with time-averaged interactions that have a linear force-displacement relationship along the longitudinal axis and are approximated as a harmonic potential well.

Similar cohesive interactions have been observed to occur in other active, collective systems. However, such interactions

are often mediated through a fluid and thus the interaction forces on the bodies can be exerted over long distances and smoothly decay as separation increases. For example, recent work has found that the spatial arrangements of undulatory swimmers inspired from fish schools are cohesive, with a strength of interaction that is dependent on the actuation dynamics and spatial positioning [68,69]. Linear perturbations of these simple swimmers yielded linear interaction forces that were approximated as harmonic potentials [68,69]. Experiments with tandem undulating foils also demonstrate stable spatial configurations of the foils mediated through fluid mechanics [13] and stable but discrete swimming speeds [14]. A fundamental difference in contact-coupled systems is that, once out of reach, interactions can no longer occur. In theory long-slender swimmers in gait compatibility could be infinitesimally close and yet not have any physical interactions because they do not make contact.

This work was inspired in part by the observations of small undulatory worms and their collective swimming behavior when in close proximity. Pairs of the nematode *C. elegans* were studied in a confined channel (much like in the experiments reported here) and were observed to adjust their undulatory gait to match their neighbor's gait [48]. The authors in that work argue that the nematodes are too large for hydrodynamics to be important and thus it must be contact that is driving the gait dynamics. We acknowledge there are competing theories for why such synchronization occurs in these worms [70], and that close-range fluid interactions may be important; however, these counterpoints do not contradict the work we have presented here. Similar collective undulatory gaits have been observed in the vinegar eels (*Tubatrix acetii*) [50] in which case the authors present a modified Kuramoto model that emulates the effect of steric interactions to describe the gait adjustment. In this work we do not allow for phase modulation of the swimmers, and only spatial rearrangement. However, this scenario is quite similar to the studies of infinitely long oscillating sheets that do not change undulatory phase but can realign spatially and which are commonly referred to as "synchronized" in the literature [67].

In this work we focused on planar motion because the systems we are inspired by (*C. elegans*, undulatory robots, etc.) typically move in a planar fashion. However, for example, the sidewinding motion of snakes and snake-robots [35] occurs in 3D and there might be interesting collective states associated with the interactions of the "corkscrew" shape of the sidewinders. Similarly, we focused on relatively high-density and aligned states of undulatory swimmers, a kind of "undulatory nematic state." However, at lower densities the rotational orientations of the swimmers will become important and may lead to other interesting collective states.

This work is inspired from the broad areas of active matter systems, granular materials, and robotics. The convergence of these themes has been of significant interest in recent years because the stochastic behavior of interacting robotics systems can be exploited for robust, redundant, and resilient robots. Recent studies of robotic active matter such as smarticles [71] and stochastic particles [72] have highlighted how emergent collective behavior can be designed and tuned through local contact-interaction rules. The role of contact interactions

among shape-changing active matter systems may have applications in designing collective robot swarms that operate in close proximity. Building large functional systems from many constituent parts is not new in robotics and has gone under the titles of modular, reconfigurable, and swarm robotics over the years (See Ref. [73] and [74] for reviews). However, recent connections drawn between these robotic collectives and active matter physics [75,76] suggest novel and fruitful intersections between these fields in the years to come.

## APPENDIX: SIMULATION DETAILS

We simulated the multiswimmer numerical experiments in Project CHRONO (referred to as CHRONO). CHRONO is a multiphysics dynamics engine that handles rigid body dynamics and contact. The source code is freely available [77] and CHRONO simulations have been validated against several experiments and comparisons with other numerical solvers for accuracy [62]. Our simulations took place in CHRONO version 5.0.0.

A multibody physics solver is used to model the rigid body dynamics of multibody systems coupled together through kinematic constraints. CHRONO treats the generalized position  $\mathbf{q}$  and velocity vectors  $\dot{\mathbf{q}}$  of rigid bodies from a Cartesian approach, where the generalized position is the location of each body's center of mass in the absolute coordinate system. The multibody dynamics in the absence of friction are described by the following set of equations:

$$\mathbf{g}(\mathbf{q}, t) = \mathbf{0},$$

$$\mathbf{M}(\mathbf{q})\dot{\mathbf{v}} = \mathbf{f}(t, \mathbf{q}, \mathbf{v}) + \mathbf{G}(\mathbf{q}, t)\hat{\lambda}.$$

The first equation represents constraints between bodies, in the case of this paper, revolute joints, which are contained in the constraint equations  $\mathbf{g}(\mathbf{q}, t) = \mathbf{0}$ . The second equation defines the dynamics where  $\mathbf{M}$  is the mass matrix,  $\mathbf{f}$  are internal (i.e., Coriolis forces, joint torques) and applied forces, and  $\mathbf{G}(\mathbf{q}, t)\hat{\lambda}$  represents the constraint reaction forces.

The forces applied to the bodies may also include contact forces that "appear" and "disappear" when contact between bodies are made or broken. In the implementation in this work, contact is handled through the discrete element method using a complementarity approach (DEM-C). The complementarity approach models contact interactions as "rigid" contacts which cannot penetrate each other. This is in contrast to penalty DEM methods that model contact through elasticity and small body overlap (with elastic repulsive force). These approaches have been compared in the literature [63]. The complementarity approach poses and solves a complementarity optimization at each time step. The complementarity problem specifies that between every body, either a nonzero gap distance exists, or a nonzero contact force exists. The details of how this complementarity problem is posed and solved are described in Tasora *et al.* [62], and Heyn *et al.* [64].

The time stepper (time integrator) used in our simulation is the linear implicit Euler method. The step size of this integrator is 0.005 s. A solver is used to compute the unknown accelerations and reaction forces at each time step of the simulation. We are using the default *PSOR*, an iterative solver based on projective fixed-point method, with over

TABLE I. Simulation parameters.

Name	Variable	Value
Body length	$l$	162 mm
Body width	$w$	15 mm
Body height	$h$	30 mm
Body mass	$m$	73 g
Control P gain	$K_P$	0.15 N m/rad
Torque saturation	$T_s$	1.5 N m
Joint amplitude	$\beta_0$	40°
Joint frequency	$f$	0.5 Hz
Drag coefficient	$c_d$	1

relaxation and immediate variable update as in successive over-relaxation (SOR) methods.

We implemented viscous drag forces acting on each link of the simulated swimmers. The viscous drag forces were applied to the center of mass of each link. The drag equations are those provided in Hatton *et al.* [40]:

$$F_{i,x} = \int_{-L}^L \frac{1}{2} c_d \xi_{i,x} d\ell = c_d L \xi_{i,x},$$

$$F_{i,y} = \int_{-L}^L c_d \xi_{i,y} d\ell = 2c_d L \xi_{i,y},$$

$$M_i = \int_{-L}^L c_d \ell (\ell \xi_{i,\theta}) d\ell = \frac{2}{3} c_d L^3 \xi_{i,\theta},$$

where  $F_{i,x}$  and  $F_{i,y}$  are respectively the longitudinal and lateral forces,  $M_i$  is the moment,  $c_d$  is the differential viscous drag constant, and  $\xi_i = [\xi_{i,x}, \xi_{i,y}, \xi_{i,\theta}]^T$  is the body velocity of the center of the  $i$ th link with respect to the stationary fluid [65].

Details of simulation parameters are listed in Table I.

- [1] T. Vicsek and A. Zafeiris, *Phys. Rep.* **517**, 71 (2012).
- [2] S. Ramaswamy, *Annu. Rev. Condens. Matter Phys.* **1**, 323 (2010).
- [3] H. P. Zhang, A. Be'er, E.-L. Florin, and H. L. Swinney, *Proc. Natl. Acad. Sci. USA* **107**, 13626 (2010).
- [4] A. Be'er and G. Ariel, *Mov. Ecol.* **7**, 9 (2019).
- [5] D. H. Kelley and N. T. Ouellette, *Sci. Rep.* **3**, 1073 (2013).
- [6] J. Buhl, D. J. T. Sumpter, I. D. Couzin, J. J. Hale, E. Despland, E. R. Miller, and S. J. Simpson, *Science* **312**, 1402 (2006).
- [7] Y. Katz, K. Tunström, C. C. Ioannou, C. Huepe, and I. D. Couzin, *Proc. Natl. Acad. Sci. USA* **108**, 18720 (2011).
- [8] K. Tunström, Y. Katz, C. C. Ioannou, C. Huepe, M. J. Lutz, and I. D. Couzin, *PLoS Comput. Biol.* **9**, e1002915 (2013).
- [9] M. Castellana, W. Bialek, A. Cavagna, and I. Giardina, *Phys. Rev. E* **93**, 052416 (2016).
- [10] A. Cavagna, A. Cimarelli, I. Giardina, G. Parisi, R. Santagati, F. Stefanini, and M. Viale, *Proc. Natl. Acad. Sci. USA* **107**, 11865 (2010).
- [11] M. Ballerini, N. Cabibbo, R. Candelier, A. Cavagna, E. Cisbani, I. Giardina, V. Lecomte, A. Orlandi, G. Parisi, A. Procaccini, M. Viale, and V. Zdravkovic, *Proc. Natl. Acad. Sci. USA* **105**, 1232 (2008).
- [12] M. Nagy, Z. Akos, D. Biro, and T. Vicsek, *Nature (London)* **464**, 890 (2010).
- [13] J. W. Newbolt, J. Zhang, and L. Ristroph, *Proc. Natl. Acad. Sci. USA* **116**, 2419 (2019).
- [14] A. D. Becker, H. Masoud, J. W. Newbolt, M. Shelley, and L. Ristroph, *Nat. Commun.* **6**, 8514 (2015).
- [15] S. J. Portugal, T. Y. Hubel, J. Fritz, S. Heese, D. Trobe, B. Voelkl, S. Hailes, A. M. Wilson, and J. R. Usherwood, *Nature (London)* **505**, 399 (2014).
- [16] L. Li, M. Nagy, J. M. Graving, J. Bak-Coleman, G. Xie, and I. D. Couzin, *Nat. Commun.* **11**, 5408 (2020).
- [17] H. Moore, K. Dvoráková, N. Jenkins, and W. Breed, *Nature (London)* **418**, 174 (2002).
- [18] J. Elgeti, R. G. Winkler, and G. Gompper, *Rep. Prog. Phys.* **78**, 056601 (2015).
- [19] Y. Yang, J. Elgeti, and G. Gompper, *Phys. Rev. E* **78**, 061903 (2008).
- [20] M. R. Shaebani, A. Wysocki, R. G. Winkler, G. Gompper, and H. Rieger, *Nat. Rev. Phys.* **2**, 181 (2020).
- [21] J. Deseigne, O. Dauchot, and H. Chaté, *Phys. Rev. Lett.* **105**, 098001 (2010).
- [22] I. S. Aranson, D. Volfson, and L. S. Tsimring, *Phys. Rev. E* **75**, 051301 (2007).
- [23] A. Kudrolli, G. Lumay, D. Volfson, and L. S. Tsimring, *Phys. Rev. Lett.* **100**, 058001 (2008).
- [24] M. Bär, R. Großmann, S. Heidenreich, and F. Peruani, *Annu. Rev. Condens. Matter Phys.* **11**, 441 (2020).
- [25] A. Bricard, J.-B. Caussin, N. Desreumaux, O. Dauchot, and D. Bartolo, *Nature (London)* **503**, 95 (2013).
- [26] F. Ginelli, F. Peruani, M. Bär, and H. Chaté, *Phys. Rev. Lett.* **104**, 184502 (2010).
- [27] G. Wang, T. V. Phan, S. Li, M. Wombacher, J. Qu, Y. Peng, G. Chen, D. I. Goldman, S. A. Levin, R. H. Austin, and L. Liu, *Phys. Rev. Lett.* **126**, 108002 (2021).
- [28] J. Aguilar, D. Monaenkova, V. Linevich, W. Savoie, B. Dutta, H.-S. Kuan, M. D. Betterton, M. A. D. Goodisman, and D. I. Goldman, *Science* **361**, 672 (2018).
- [29] A. Campo, A. Gutiérrez, S. Nouyan, C. Pinciroli, V. Longchamp, S. Garnier, and M. Dorigo, *Biol. Cybern.* **103**, 339 (2010).
- [30] T. Vicsek, A. Czirók, E. Ben-Jacob, I. Cohen, I. and O. Shochet, *Phys. Rev. Lett.* **75**, 1226 (1995).
- [31] E. A. Gaffney, H. Gadélha, D. J. Smith, J. R. Blake, and J. C. Kirkman-Brown, *Ann. Rev. Fluid Mech.* **43**, 501 (2011).
- [32] J. Gray and H. W. Lissmann, *J. Exp. Biol.* **26**, 354 (1950).
- [33] D. L. Hu, J. Nirody, T. Scott, and M. J. Shelley, *Proc. Natl. Acad. Sci. USA* **106**, 10081 (2009).
- [34] Z. V. Guo and L. Mahadevan, *Proc. Natl. Acad. Sci. USA* **105**, 3179 (2008).
- [35] H. Marvi, C. Gong, N. Gravish, H. Astley, M. Travers, R. L. Hatton, J. R. Mendelson, 3rd, H. Choset, D. L. Hu, and D. I. Goldman, *Science* **346**, 224 (2014).
- [36] E. M. Purcell, *Am. J. Phys.* **45**, 3 (1977).

- [37] L. E. Becker, S. A. Koehler, and H. A. Stone, *J. Fluid Mech.* **490**, 15 (2003).
- [38] F. Jing and S. Alben, *Phys. Rev. E* **87**, 022711 (2013).
- [39] S. Alben, *Phys. Rev. E* **103**, 042414 (2021).
- [40] R. L. Hatton, Y. Ding, H. Choset, and D. I. Goldman, *Phys. Rev. Lett.* **110**, 078101 (2013).
- [41] D. Tam and A. E. Hosoi, *Phys. Rev. Lett.* **98**, 068105 (2007).
- [42] O. Wiesel and Y. Or, *Proc. R. Soc. London, Ser. A* **472**, 20160425 (2016).
- [43] J. M. Rieser, C. Gong, H. C. Astley, P. E. Schiebel, R. L. Hatton, H. Choset, and D. I. Goldman, *arXiv:1906.11374*.
- [44] J. M. Rieser, P. E. Schiebel, A. Pazouki, F. Qian, Z. Goddard, K. Wiesenfeld, A. Zangwill, D. Negrut, and D. I. Goldman, *Phys. Rev. E* **99**, 022606 (2019).
- [45] V. Kantsler, J. Dunkel, M. Polin, and R. E. Goldstein, *Proc. Natl. Acad. Sci. USA* **110**, 1187 (2013).
- [46] G. Juarez, K. Lu, J. Sznitman, and P. E. Arratia, *Europhys. Lett.* **92**, 44002 (2010).
- [47] S. Park, H. Hwang, S.-W. Nam, F. Martinez, R. H. Austin, and W. S. Ryu, *PLoS One* **3**, e2550 (2008).
- [48] J. Yuan, D. M. Raizen, and H. H. Bau, *Proc. Natl. Acad. Sci. USA* **111**, 6865 (2014).
- [49] A. Peshkov, S. McGaffigan, and A. C. Quillen, *Soft Matter* **18**, 1174 (2022).
- [50] A. C. Quillen, A. Peshkov, E. Wright, and S. McGaffigan, *Phys. Rev. E* **104**, 014412 (2021).
- [51] S. Immler, H. D. M. Moore, W. G. Breed, and T. R. Birkhead, *PLoS One* **2**, e170 (2007).
- [52] Y. Yang, V. Marceau, and G. Gompper, *Phys. Rev. E* **82**, 031904 (2010).
- [53] R. E. Goldstein, M. Polin, and I. Tuval, *Phys. Rev. Lett.* **103**, 168103 (2009).
- [54] D. R. Brumley, N. Bruot, J. Kotar, R. E. Goldstein, P. Cicuta, and M. Polin, *Phys. Rev. Fluids* **1**, 081201(R) (2016).
- [55] D. R. Brumley, K. Y. Wan, M. Polin, and R. E. Goldstein, *eLife* **3**, e02750 (2014).
- [56] H. Guo, L. Fauci, M. Shelley, and E. Kanso, *J. Fluid Mech.* **836**, 304 (2018).
- [57] J. Kotar, M. Leoni, B. Bassetti, M. C. Lagomarsino, and P. Cicuta, *Proc. Natl. Acad. Sci. USA* **107**, 7669 (2010).
- [58] R. Chelakkot, M. F. Hagan, and A. Gopinath, *Soft Matter* **17**, 1091 (2021).
- [59] S. Y. Reigh, R. G. Winkler, and G. Gompper, *Soft Matter* **8**, 4363 (2012).
- [60] Y. Ozkan-Aydin, D. I. Goldman, and M. S. Bhamla, *Proc. Natl. Acad. Sci. USA* **118** (2021).
- [61] See Supplemental Material at <http://link.aps.org/supplemental/10.1103/PhysRevE.105.054604> for examples of three-link robot experiment and simulation.
- [62] A. Tasora, R. Serban, H. Mazhar, A. Pazouki, D. Melanz, J. Fleischmann, M. Taylor, H. Sugiyama, and D. Negrut, *High Performance Computing in Science and Engineering*, edited by T. Kozubek, R. Blaheta, J. Šístek, M. Rozložník, and M. Čermák (Springer International Publishing, Cham, 2016), pp. 19–49.
- [63] A. Pazouki, M. Kwarta, K. Williams, W. Likos, R. Serban, P. Jayakumar, and D. Negrut, *Phys. Rev. E* **96**, 042905 (2017).
- [64] T. Heyn, D. Negrut, M. Anitescu, A. Tasora, and D. Lamb, in *ASME 2012 International Design Engineering Technical Conferences and Computers and Information in Engineering Conference, Chicago, Illinois, USA* (American Society of Mechanical Engineers Digital Collection, 2013), pp. 61–69.
- [65] R. L. Hatton and H. Choset, *IEEE Trans. Robot.* **29**, 615 (2013).
- [66] V. Narayan, S. Ramaswamy, and N. Menon, *Science* **317**, 105 (2007).
- [67] G. J. Elfring and E. Lauga, *Phys. Rev. Lett.* **103**, 088101 (2009).
- [68] S. Heydari and E. Kanso, *arXiv:2009.12715*.
- [69] S. Ramanarivo, F. Fang, A. Oza, J. Zhang, and L. Ristroph, *Phys. Rev. Fluids* **1**, 071201(R) (2016).
- [70] T. Chakraborty, A. Suman, A. Gupta, V. Singh, and M. Varma, *Phys. Rev. E* **99**, 052410 (2019).
- [71] W. Savoie, T. A. Berrueta, Z. Jackson, A. Pervan, R. Warkentin, S. Li, T. D. Murphey, K. Wiesenfeld, and D. I. Goldman, *Sci. Robot.* **4**, eaax4316 (2019).
- [72] S. Li, R. Batra, D. Brown, H.-D. Chang, N. Ranganathan, C. Hoberman, D. Rus, and H. Lipson, *Nature (London)* **567**, 361 (2019).
- [73] J. Seo, J. Paik, and M. Yim, *Ann. Rev. Control, Robotics, Autonomous Sys.* **2**, 63 (2019).
- [74] M. Brambilla, E. Ferrante, M. Birattari, and M. Dorigo, *Swarm Intell.* **7**, 1 (2013).
- [75] M. Fruchart, R. Hanai, P. B. Littlewood, and V. Vitelli, *Nature (London)* **592**, 363 (2021).
- [76] P. Chvykov, T. A. Berrueta, A. Vardhan, W. Savoie, A. Samland, T. D. Murphey, K. Wiesenfeld, D. I. Goldman, and J. L. England, *Science* **371**, 90 (2021).
- [77] Code can be found on the Project CHRONO github page (<https://github.com/projectchrono/chrono>).